



# Thermo-acoustic velocity coupling in a swirl stabilized gas turbine model combustor



Vincent Caux-Brisebois <sup>a</sup>, Adam M. Steinberg <sup>a,\*</sup>, Christoph M. Arndt <sup>b</sup>, Wolfgang Meier <sup>b</sup>

<sup>a</sup> Institute for Aerospace Studies, University of Toronto, 4925 Dufferin Street, Toronto, Ontario M3H 5T6, Canada

<sup>b</sup> Institute of Combustion Technology, German Aerospace Center (DLR), D-70569 Stuttgart, Baden-Württemberg, Germany

## ARTICLE INFO

### Article history:

Received 12 March 2014

Received in revised form 16 May 2014

Accepted 21 May 2014

Available online 26 June 2014

### Keywords:

Premixed turbulent combustion

Thermo-acoustic coupling

Combustion instability

## ABSTRACT

Limit-cycle thermo-acoustic velocity coupling mechanisms are studied in a perfectly-premixed swirl-stabilized combustor using data from 10 kHz repetition-rate stereoscopic particle image velocimetry (S-PIV) and OH planar laser induced fluorescence (PLIF). Five cases over a range of thermal powers and equivalence ratios were investigated, each of which underwent different amplitude limit-cycle oscillations. Proper orthogonal decomposition (POD) of the velocity data showed that each case contained a dynamic helical vortex core (HVC) that rotated around the combustor and greatly affected the flame behavior. Flow and flame statistics were compiled as a function of both the phase in the thermo-acoustic cycle and a phase representing the azimuthal position of the HVC relative to the measurement plane. These data were used to determine the thermo-acoustic energy transfer field at each HVC azimuthal angle, as described by the Rayleigh integral. It was found that periodic deformations of the HVC caused large-scale flame motions, resulting in regions of positive and negative energy transfer. The deformation of the HVC was linked to a swirl number wave that propagated from the burner nozzle. While the mechanism of thermo-acoustic coupling was the same for all cases, the phase between heat release and pressure oscillations varied significantly. This phase relationship was determined by the interaction of the pressure field, swirl wave, HVC deformation, and flame response. It was shown that these can be described by the combination of a Helmholtz resonator and a convective disturbance.

© 2014 The Combustion Institute. Published by Elsevier Inc. All rights reserved.

## 1. Introduction

This paper presents an analysis of the fluid mechanical mechanisms driving self-excited limit-cycle thermo-acoustic oscillations in a gas turbine model combustor (GTMC) burning swirl-stabilized lean-premixed (LP) flames. Natural excitation of thermo-acoustic oscillations is a major problem in modern gas turbine combustors, which often employ LP combustion in order to reduce NO<sub>x</sub> emissions [1–3]. The local volumetric heat release rate ( $\dot{q}$ ) from such flames is highly sensitive to various perturbations, particularly fluctuations in the flow field and reactant mixture composition [4]. The former, often referred to as velocity-coupling, leads to changes in the amount and distribution of reactive surface area through flame wrinkling, stretch, ignition, and extinction, whereas the latter changes the heat release rate per unit flame area. Periodic oscillations in both the flow field and reactant mixture can be generated by pressure ( $p$ ) oscillations, which results in coupling between combustion and pressure.

Local pressure-combustion coupling is described by the Rayleigh integral

$$\theta(\mathbf{x}) = \frac{\gamma - 1}{\gamma} \frac{1}{\bar{p}} \int_t p'(\mathbf{x}, t) \dot{q}'(\mathbf{x}, t) dt \quad (1)$$

where  $\theta$  represents the local rate of energy transfer from heat release oscillations to pressure oscillations and  $(\cdot)'$  is the local fluctuation relative to the mean  $(\cdot)$ . Positive values of  $\theta$  indicate that the local coupling drives the oscillations (in-phase pressure and heat-release oscillations), whereas negative  $\theta$  indicates local damping (out-of-phase oscillations).

Steady-state limit-cycle amplitudes are reached when the net energy transfer in the combustor volume equals the rate at which acoustic energy is transmitted and dissipated by the system [5]. Practical LP gas turbine combustors can exhibit limit-cycle amplitudes at particular conditions that are sufficient to cause major hardware damage, reduced combustion efficiency, increased emissions, and/or global flame extinction through blow-off or flashback. Several control strategies have been devised to mitigate thermo-acoustic instabilities [5–8], though these generally are applied as retrofits to specific combustor models when instabilities

\* Corresponding author.

E-mail address: [steinberg@utias.utoronto.ca](mailto:steinberg@utias.utoronto.ca) (A.M. Steinberg).

## Nomenclature

Symbols			
$A_s$	area of swirler for Helmholtz resonator analysis	$\Psi$	total thermo-acoustic energy transfer from doubly-phase-resolved analysis
$a$	POD temporal coefficient	$\omega$	vorticity
$b$	damping constant in Helmholtz resonator analysis		
$f$	frequency		
$k$	stiffness constant in Helmholtz resonator analysis		
$M$	POD eigenmode		
$m_s$	mass of fluid in swirler for Helmholtz resonator analysis		
$N_p$	number of phases for doubly-phase-resolved analysis		
$P_{th}$	thermal power		
$S$	Swirl number		
$v_s$	convective velocity of swirl wave		
Greek			
$\theta$	local thermo-acoustic energy transfer	$(\cdot)'$	instantaneous fluctuation
$\Sigma$	flame surface density	$(\cdot)''$	root-mean-square fluctuation
$\varphi$	equivalence ratio	$(\cdot)$	time average
$\phi$	phase angle in oscillation	$\{\cdot\}$	property integrated across the field of view
$\psi$	local thermo-acoustic energy transfer from doubly-phase-resolved analysis	$\langle \cdot \rangle$	property integrated across the field of view width ( $x$ ) at a particular $y$
		$(\cdot)^{ah}$	doubly-phase-resolved component (Eq. (3))
		$(\cdot)^t$	turbulent fluctuation relative to doubly-phase-resolved mean (Eq. (3))
		$(\bar{\cdot})^{ah}$	doubly-phase-resolved mean (sum of mean and doubly-phase-resolved component) (Eq. (4))
		$(\cdot)^a$	doubly-phase-resolved oscillation relative to mean over the acoustic cycle (Eq. (5))

are encountered, and are not broadly robust to changes in configuration or operating parameters. The complexity of the driving acoustic/flow/combustion interactions currently makes prediction and efficient control of unstable conditions extremely challenging, particularly in engine-relevant combustors. Doing so requires better understanding of the flow–flame–acoustic interactions driving practical oscillations.

Many investigations have been performed of thermo-acoustic coupling in LP combustion systems, ranging from simple laminar flames to complex gas turbine combustors [9–17]. The response of a flame to perturbations often is represented by a flame transfer function (FTF), which describes the linear response of the system to low-amplitude forcing. Non-linear flame describing functions (FDF) also have been investigated that allow consideration of higher amplitude disturbances [18,19]. FTFs (and FDFs) can be experimentally determined in a combustor geometry of interest by operating the combustor over a range of conditions and, at each condition, forcing the system at a variety of frequencies (and amplitudes). The resulting transfer functions can then be used to determine the unstable modes of the combustor through a dispersion relationship and, in the case of an FDF, may allow estimation of the limit cycle amplitude. However, this approach requires experimental testing of the combustor over a wide set of conditions and forcing parameters, making their application to the design process challenging. Moreover, it is unclear whether the coupling mechanisms initiating instabilities at low perturbation amplitudes persist in high-amplitude limit cycle oscillations.

It therefore is desirable to have a better mechanistic understanding of finite-amplitude thermo-acoustic velocity coupling mechanisms. For simple flames, such as laminar V-flames and conical flames, analytical methods exist that can predict linear FTFs with reasonable accuracy using a flame-sheet approach [20–27]. In these methods, acoustically generated velocity disturbances affect the local heat release oscillations by altering the kinematic balance between flame propagation and the surface-normal flow velocity [28]. Different types of disturbance convect at different velocities, e.g. shed-vortex induced flame wrinkling or bulk flow oscillations, resulting in a spatially distributed phase relationship between the heat release oscillations and acoustics that depends on the flame geometry and disturbance convective-velocities.

In more complex swirl-stabilized flames, models for the FTF in systems undergoing low-amplitude forcing have recently been investigated. Palies et al. [19,29] studied a swirl-stabilized premixed flame using the G-equation and found that the FTF had a similar form to that for an inverted conical V-flame, with some alterations due to differences in convective velocities of axial and azimuthal disturbances. Jones et al. [30] experimentally studied a premixed swirl flame undergoing velocity forcing at an amplitude of 5%. They found two flame perturbation mechanisms, one driven by shed-vortices that propagated along the flame from the anchoring point, and the other generated in the outer-shear layer.

However, the velocity coupling mechanisms that occur during high-amplitude self-excited oscillations may be considerably different. For example, a commonly reported low-amplitude convective disturbance is associated with periodic vortex shedding from the combustor dump-plane causing flame wrinkles that propagate up the flame [31–33]. However, it has been shown that intense swirl flames often do not exhibit such shedding, but may instead contain three-dimensional helical vortex cores (HVC) that rotate around the burner at a frequency that is different than the acoustics [34–43]. While the conditions leading to the formation of HVCs remain unclear, parameters such as the mass flow rate, combustor geometry, and mode of premixing are known to be of importance [40,44]. Results from the burner studied here have demonstrated that conditions with high-amplitude self-excited oscillations often exhibit such HVCs, whereas conditions with low-amplitude oscillations generally exhibit periodic vortex shedding [31]. It also has been shown that rapid transition between low- and high-amplitude self-excited oscillations can be associated with rapid transition from periodic vortex shedding to an HVC [45]. Hence, the fundamental velocity coupling mechanism for high-amplitude self-excited oscillations would be very different than those found using low amplitude forcing.

In this paper, such self-excited velocity coupling mechanisms are investigated using high-repetition-rate (10 kHz) OH planar laser induced fluorescence (PLIF) and stereoscopic particle image velocimetry (S-PIV), along with acoustics measurements. The diagnostics are applied in a swirl-stabilized combustor burning perfectly premixed methane-air flames. The combustor studied is geometrically identical to a commonly studied configuration that

typically is operated in a ‘technically premixed’ mode, e.g. Ref. [37,45–51]. In the technically premixed mode, temporal and spatial fuel/air stratification occurs due to interaction of the acoustic waves with the non-stiff fuel injector. However, for the current work, a spatially and temporally constant equivalence ratio was achieved by premixing the reactants well upstream of a choked orifice, thereby isolating the thermo-acoustic velocity coupling from effects of combustion chemistry.

Previous work with other swirl-flames has shown that considerable insight into thermo-acoustic velocity coupling can be gained by resolving data from high-repetition-rate laser diagnostics with respect to both the phase in the acoustic cycle and the azimuthal position of the HVC relative to the measurement plane [31,32]. With such a ‘doubly-phase-resolved’ analysis, highly repeatable flow–flame interactions were found to occur over the acoustic cycle at each HVC azimuthal position; the nature and phase (relative to the acoustics) of the interactions depended on the position at which the HVC was being observed. It also was shown that such analysis can be used to solve a statistical analog to the Rayleigh integral of Eq. (1).

In this work, these analysis techniques are applied to a variety of perfectly-premixed methane–air flames. The data are analysed to provide new insight into thermo-acoustic velocity coupling in swirl-stabilized flames, including critical phase delays. The paper is organized as follows. In Section 2, the experimental apparatus, test conditions, and diagnostics are described. Section 3 provides an overview and demonstration of the analysis techniques employed. The thermo-acoustic energy transfer fields are presented in Section 4, along with the underlying velocity coupling mechanisms and phase relationships.

## 2. Experiment and diagnostics

### 2.1. Combustor and test conditions

The basic GTMC geometry employed for this work, shown in Fig. 1, has been the subject of numerous previous experimental and computational studies. However, with exception of Ref. [33], the experimental studies have been conducted with fuel injected directly into the swirler, resulting in ‘technical premixing’ and interactions between the acoustics and fuel supply system. Conversely, with the exception of Ref. [51], the computational studies have employed perfect premixing of the fuel and air.

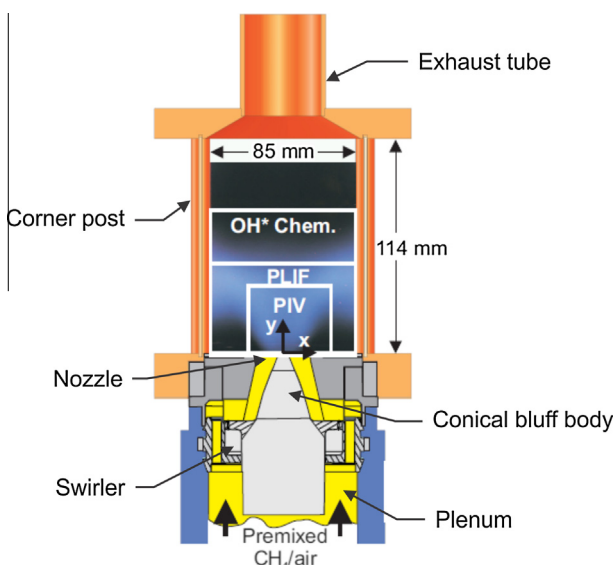


Fig. 1. Combustor schematic with diagnostic field-of-views.

The studies conducted here aim to isolate velocity-coupling and therefore were performed with perfect premixing. Fuel (CH<sub>4</sub>) and air were combined in a commercial premixer located approximately 2 m upstream of the plenum. The mixture then passed through a plate with a choked orifice, located in a 25 mm diameter tube 0.15 m upstream of the combustor plenum entrance. The diameter of the orifice was changed, depending on the operating conditions, to ensure choked flow over the plate. This configuration isolated the fuel and air supply from the combustor acoustics and provided known upstream boundary conditions.

The CH<sub>4</sub>/air mixture was fed from the 25 mm diameter tube into the combustor plenum (78 mm diameter, 100 mm length), through a radial swirler (12 swirl vanes), to the burner nozzle (27.85 mm exit diameter), and then into the combustion-chamber (85 × 85 mm cross-section, 114 mm length). The inner surface of the nozzle was formed by a conical bluff body, the tip of which was at the nozzle exit plane (nozzle inner diameter = 0 mm at  $y = 0$  mm). The combustion-chamber itself was composed of four large fused-silica windows, held in the corners by Inconel posts. The large windows provided good optical access to the combustion-chamber, allowing for the application of optical diagnostics. Further information on the combustor geometry can be found in Ref. [46].

The overall experimental program consisted of nine conditions, covering a range of thermal powers (10–35 kW) and equivalence ratios ( $\phi = 0.65–0.80$ ). However, it was shown in Ref. [33] that the cases with the largest amplitude thermo-acoustic oscillations were those that contained HVCs. These cases therefore are the subject of the current work and are summarized in Table 1. The labeling scheme for the cases is chosen to be consistent with previous work [33]. Also shown in this table are the mass flow rates ( $\dot{m}$ ) of air and fuel, root-mean-squared pressure fluctuation amplitude ( $p''$ ), dominant thermo-acoustic frequency ( $f_{ac}$ ), and rotation frequency of the HVC ( $f_h$ ). The integral length scale is set by the nozzle exit radius and the resultant characteristics place these flames in the corrugated flamelet regime of turbulent premixed combustion. All flow rates were controlled using electromechanical mass flow controllers (Brooks) and monitored using Coriolis mass flow meters (Siemens Sitrans F C) with an uncertainty of 1.5%. During a data acquisition run, approximately 5% of the air mass flow was diverted through a fluidized bed particle seeder containing TiO<sub>2</sub> particles with a diameter of approximately 1 μm to enable the S-PIV velocity measurements described below.

The system was equipped with multiple ports for pressure and temperature measurements. Pressures were measured using calibrated microphone probes (Brüel and Kjaer, Type 4939), sampled at a rate of 50 kHz. The combustion-chamber pressure was measured using two probes in a corner post, and the plenum pressure was measured using a probe flush with the plenum wall. Detailed acoustic characterization using multiple acoustic measurement ports and Comsol simulations have shown that the system operates as a Helmholtz resonator [52]. Hence, the pressure oscillations were essentially spatially uniform throughout each of the combustion and plenum chambers, with significant spatial pressure gradients only within the swirler/nozzle assembly and exhaust tube. It is noted that this Helmholtz mode is somewhat different than the longitudinal mode often studied, e.g. when determining FTFs. Data on the burner temperature boundary conditions and atmospheric conditions during data acquisition are available from the authors for simulation development.

### 2.2. Diagnostics

Simultaneous 10 kHz S-PIV and OH PLIF measurements were obtained using the high-repetition-rate laser diagnostics system at the German Aerospace Center Institute of Combustion

**Table 1**  
Experimental cases.

Case	$\varphi$	$P_{th}$ (kW)	$\dot{m}_{air}$ (g/min)	$\dot{m}_{CH_4}$ (g/min)	$p''$ (Pa)	$f_{ac}$ (Hz)	$f_h$ (Hz)
3	0.7	20	588	24.0	107.4	296	475
4	0.7	25	733	30.0	74.4	306	578
5a	0.65	30	940	36.0	145.4	289	749
5b	0.7	30	880	36.0	149.1	314	693
5c	0.75	30	824	36.0	177.2	418	747
6	0.7	35	$1.02 \times 10^3$	42.0	181.9	380	799

Technology. The S-PIV system consisted of a high-repetition-rate, dual-cavity, diode-pumped solid-state (DPSS) Nd:YAG laser (Edge-wave, IS-6IIDE) and a pair of high-speed CMOS cameras (LaVision HSS 8). Laser pulse pairs (532 nm, 2.6 mJ/pulse, 14 ns pulse duration, 5–15  $\mu$ s between pulses depending on conditions) repeating at 10 kHz were expanded into a sheet having a usable height of about 40 mm and a full-width-at-half-maximum (FWHM) of approximately 1 mm at the measurement area. Particle-scattered light from the  $TiO_2$  seed was collected into the cameras using 100 mm focal length commercial camera lenses (Tokina) set to f/5.6. The field-of-view imaged by the PIV system was approximately 49 mm  $\times$  38 mm. Due to optical access restrictions caused by the combustion chamber posts, the S-PIV field-of-view was offset from the centerline of the burner, covering the range  $x = -17$  to 32 mm. The CMOS cameras were mounted equidistantly from opposite sides of the laser sheet in a forward-scatter configuration. Standard corrections were made for image defocusing and perspective distortion using Scheimpflug adapters and a 3D dot target (LaVision Type 7). The same target images were used to align the fields-of-view from the PIV cameras with those from the PLIF and chemiluminescence cameras described below. Vector fields were computed from the particle image spatial cross-correlation using the LaVision DaVis 8.0 software package, with a final interrogation box size and vector spacing of approximately 1.0 mm and 0.5 mm respectively.

The OH PLIF system consisted of a DPSS laser (Edgewave IS8II-E) pumping a dye laser (Sirah Credo). The dye laser output was frequency doubled and tuned to excite the  $Q_1(7)$  line of the  $A - X(v' = 1, v'' = 0)$  band of OH at 283.2 nm, with a final laser energy of approximately 0.18 mJ/pulse. The laser beam was expanded into a sheet with a usable height of approximately 50 mm and a FWHM of approximately 0.4 mm at the measurement area, combined with the sheet from the PIV laser using a dichroic mirror, and transmitted through the combustor along the same beam path, as seen in the configuration schematic of Fig. 2. The PLIF laser pulse occurred between PIV laser pulses for each velocity field. Fluorescence of the OH radical in the range of 310 nm was acquired with a CMOS camera (LaVision HSS5) equipped with an external, two-stage, lens-coupled intensifier (LaVision HS-IRO)

and a 45 mm f/1.8 UV lens (Cerco). The field-of-view of the PLIF system covered the entire width of the combustion chamber (85 mm) and extended from the nozzle exit to a height of 50 mm. Background luminosity and elastic scattering were reduced by using a short intensifier gate (100 ns) and a high-transmission (greater than 80% at 310 nm) bandpass interference filter (Laser Components GmbH). The OH images were corrected for the mean laser sheet intensity profile, which was determined based on 1000 images of the fluorescence from a uniform acetone vapor that was doped into the test area, as well as the whitefield response. The PLIF images were filtered with a 0.4 mm Gaussian filter (same width as the sheet thickness) prior to further analysis to reduce high-frequency pixel noise. This sheet thickness and filter width set the effective spatial resolution of the PLIF images.

A minimum of two independent data acquisitions were conducted at each condition, resulting in over 15,000 individual measurements of a given flame. This quantity of data allowed for convergence of the doubly-phase-resolved statistical analysis described in Section 3.2.

### 3. Data analysis

The objective of this work is to understand the mechanisms controlling self-excited thermo-acoustic coupling in swirl-stabilized GTMC systems, *viz.* Eq. (1). However, doing so is complicated by the dynamic 3D nature of the flow and flame. That is, solution of the Eq. (1) requires knowledge of the volumetric heat release fluctuation distribution in space and time relative to the acoustics. Due to the 3D asymmetries associated with the HVC in the studied flames, these heat release oscillations did not occur in radially symmetric patterns, but in a spiraling pattern set by the HVC shape and position. Hence, understanding the thermo-acoustic coupling requires observation of oscillatory flow–flame interactions (*i.e.* over the acoustic cycle) that occur at a particular azimuthal location along the HVC; without considering the HVC position, evaluation of the Rayleigh integral does not elucidate the actual flow–flame interactions driving the oscillations.

A mathematical framework for performing such an analysis was described in Refs. [31,32] and is summarized below. The analysis consists of three major steps;

1. Quantification of the HVC azimuthal position relative to the measurement plane using proper orthogonal decomposition (POD).
2. Determination of the oscillatory flame and flow behavior over the thermo-acoustic cycle at each HVC azimuthal position using doubly-phase-resolved analysis.
3. Solution of a statistical analog to the Rayleigh integral (Eq. (1)) to determine the thermo-acoustic energy transfer distribution at each HVC azimuthal location.

Subsequently, the doubly-phase-resolved statistical flow and flame data will be used to elucidate the mechanisms setting the thermo-acoustic energy transfer fields.

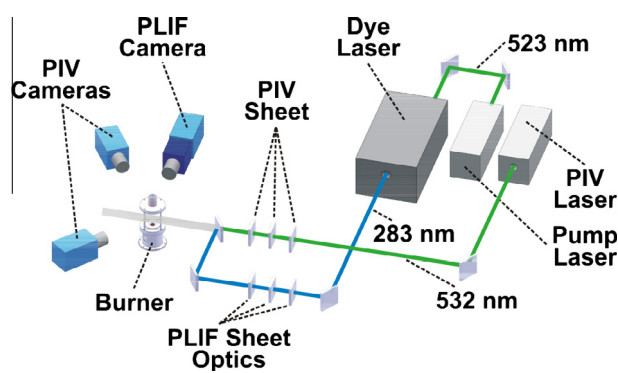


Fig. 2. Layout of 10 kHz PLIF and S-PIV systems.

### 3.1. Proper orthogonal decomposition

POD is becoming an increasingly popular method of analysing coherent structures in turbulent flow and turbulent combustion [31–33]. In POD, a sequence of individual measurements is used to construct an orthogonal basis for the data, such that the measurement at any given time can be expressed as a linear combination of the basis modes. While numerous orthogonal bases can be derived, the POD basis is chosen to be the eigenmodes of the original data (i.e. from the singular value decomposition). This basis has the particular property of providing optimal convergence of the system energy; the energy contained in the most energetic eigenmode is the most energetic mode of any basis, and similarly for the subsequent modes. As a consequence, the energetic modes of the POD basis can be used to represent the most energetic flow features. In systems with coherent structures, the most energetic POD modes tend to represent these structures and their behavior can be isolated from stochastic processes by appropriately summing the energetic modes. In the full POD, the number of eigenmodes equals the number of instantaneous measurements used to construct the POD. However, performing such an analysis is very computationally expensive and unnecessary when only the most energetic modes are needed. Here, a block-Lanczos method was used to generate only the most energetic modes of the POD [53].

Mathematically, POD analysis from a sequence of  $n$  temporally resolved 2D measurements taken at  $t_i | 1 \leq i \leq n$  provides a set of  $m \leq n$  spatial eigenmodes ( $M_j(x, y)$ ), coefficients ( $a_j(t_i)$ ), and eigenvalues ( $\lambda_j$ ). The coefficients represent the instantaneous contribution of each basis mode to the original data at a particular  $t_i$ . If the data is taken with sufficient repetition-rate to resolve the system dynamics,  $a_j(t_i)$  evolve in a coherent fashion with time. The eigenvalues represent the net contribution of each mode to the overall energy of the data; POD modes are arranged such that  $\lambda_1 > \lambda_2 > \dots > \lambda_m$ . It is common practice in the application of POD to center the data about the mean such that the first (most energetic) mode represents a fluctuation. The temporal history of the data from the  $k$  most dominant modes is then given by

$$\zeta_k(x, y, t_i) = \bar{\zeta}(x, y) + \sum_{j=0}^k a_j(t_i) M_j(x, y) \quad (2)$$

It previously has been shown that the most energetic POD modes in the studied flames represent the structure and dynamics of the HVC. This is demonstrated in Figs. 3 and 4, which show the POD reconstruction of the flow field for Case 6. The POD modes used to construct these images contained over 65% of the total turbulent kinetic energy of the flow. For the image sequence of Fig. 3, the velocity field was reconstructed from the ten most energetic

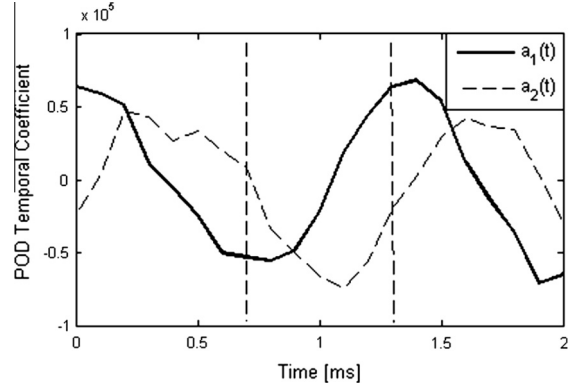


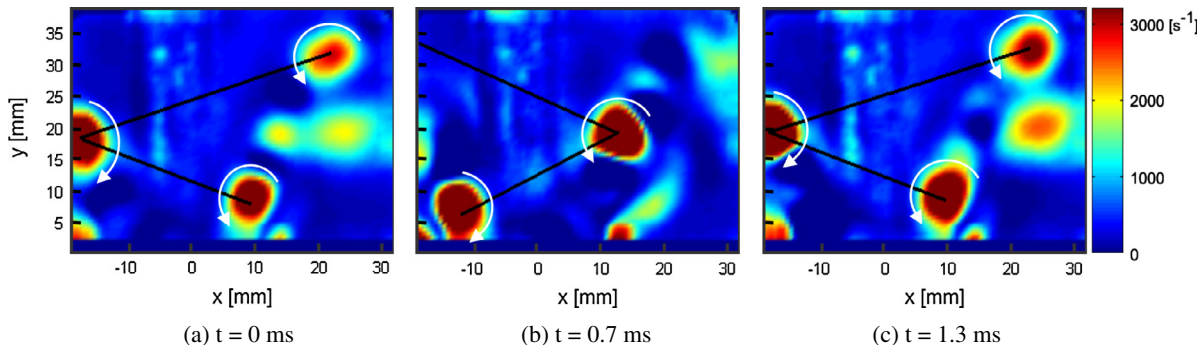
**Fig. 4.** Evolution of  $a_1(t)$  and  $a_2(t)$  over the time span shown in Fig. 3. Dashed lines are at  $t = 0$ ,  $t = 0.7$ , and  $t = 1.3$  ms, corresponding to the times in Fig. 3.

POD modes (i.e.  $\bar{u}_{10}(x, y)$ ), from which the 2D swirling strength field was calculated. The swirling strength is a robust means of visualizing flow regions in which the local velocity field is rotating in a frame moving with the flow. Mathematically, it is defined as the magnitude of the complex components of the eigenvalues of the velocity gradient tensor. Unlike vorticity, the swirling strength field does not include regions of high shear and hence produces clearer images of the HVC. It is noted that the intersection of a helical vortex in a 2D measurement results in the staggered pattern of vortices, which appear as nearly circular regions of high swirling strength in the figure.

Figure 4 shows the temporal coefficient of the first two POD modes,  $a_1(t)$  and  $a_2(t)$ , over the time period of Fig. 3. As can be seen, the POD coefficients represent the azimuthal location of the HVC with respect to the measurement plane. Over half an oscillation of the POD coefficient, the HVC rotated half way around the burner, resulting in the mirrored images between  $t = 0$  and  $t = 0.7$  s. As the coefficients completed their oscillation, the HVC returned to its original azimuthal position. Hence, the POD coefficients can be used to identify the azimuthal position of the HVC with respect to the measurement plane. It is noted that usage of the POD coefficient results in a somewhat arbitrary zero-point for the azimuthal HVC position; for this work, the beginning of the HVC cycle will correspond to local maxima of  $a_1(t)$  [31,33,54].

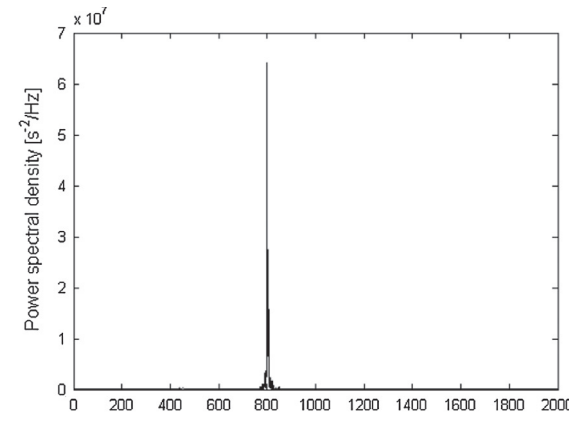
### 3.2. Doubly-phase-resolved analysis

Table 1 shows the frequencies of the HVC motion around the burner and the dominant thermo-acoustic oscillation, which were calculated by fast Fourier transformation of  $a_1(t)$  and the microphone signal, respectively. Examples of the power spectra for these

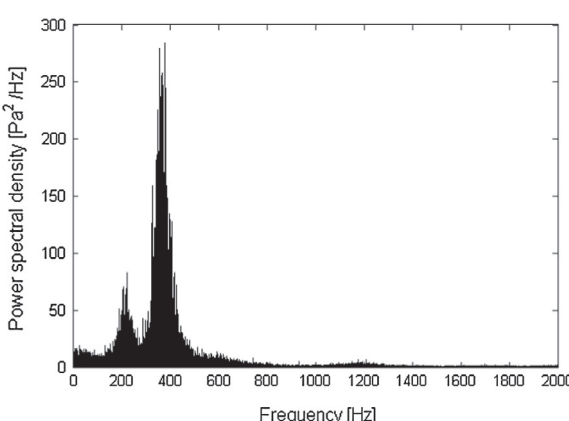


**Fig. 3.** Instantaneous sequence showing the swirling strength reconstructed from the 10 first POD modes for the loudest case (Case 6). The staggered arrangement of the counter-rotating vortices is characteristic of the helical vortex core.

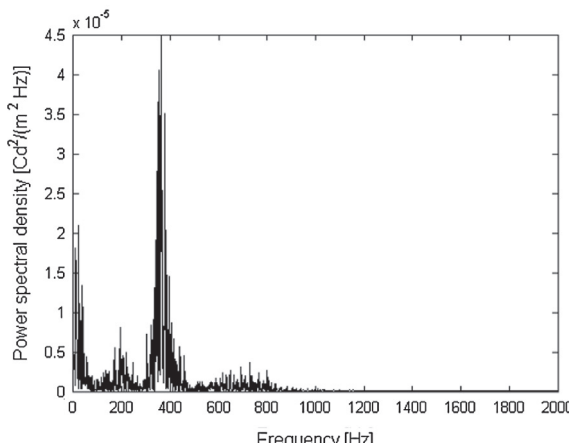
signals, along with the overall heat release as characterized by the total OH<sup>+</sup> chemiluminescence (captured using an identical imaging arrangement to the PLIF system), are provided in Fig. 5. As can be seen, the pressure and heat release oscillations had similar power spectra, while the HVC and pressure oscillations had considerably different frequencies for each case; it was shown in Ref. [33] that the HVC frequency increased linearly with flow rate, corresponding to a constant Strouhal number, as expected for the precession of a vortex core.



(a) PSD of the first POD swirl mode ( $a_1(t)$ )



(b) PSD of the chamber acoustic signal



(c) PSD of the chemiluminescence signal

**Fig. 5.** Power spectra of the  $a_1(t)$ , the chamber acoustics, and the heat release oscillations for Case 6. While the heat release oscillated at the same frequency as the acoustics, the HVC circumscribed the burner at a much higher rate.

In order to understand the thermo-acoustically coupled flame and flow oscillations over the acoustic cycle, it therefore is necessary to resolve the measurements with respect to both the phase in the thermo-acoustic cycle and the HVC azimuthal position with respect to the measurement plane, i.e. through a doubly-phase-resolved analysis. That is, at each HVC azimuthal position, repeatable oscillatory flow-flame interactions occur over the thermo-acoustic cycle [31,33]. These interactions are critical in setting the oscillatory flame dynamics, and hence the thermo-acoustic energy transfer fields.

Mathematically, it is useful to define several quantities related to the doubly-phase-resolved analysis. Any instantaneous measurement ( $\zeta$ ) can be decomposed into its long-time average ( $\bar{\zeta}$ ), a mean doubly-phase-resolved mean component in excess of the long-time average ( $\zeta^{ah}$ ), and a stochastic (turbulent) fluctuation ( $\zeta^t$ ), such that

$$\zeta(x, y, t) = \bar{\zeta}(x, y) + \zeta^{ah}(x, y, \phi_a(t), \phi_h(t)) + \zeta^t(x, y, t) \quad (3)$$

where  $\phi_a$  and  $\phi_h$  are the phases in the thermo-acoustic and HVC cycles at the measurement time  $t$ , respectively. For this work, the  $\phi_a$  and  $\phi_h$  at a particular time were determined by dividing their respective oscillatory signals into  $N_p = 12$  discrete phase numbers, as shown in Fig. 6, resulting in 144 phase combination pairs. Each measurement was then associated with the closest combination of discrete phases. A typical measurement sequence consisted of approximately 8000 images, resulting in 50–60 images at each phase angle combination. Two measurement sequences were used at each condition (100–120 images per phase combination), which was sufficient to obtain well converged statistics.

An important quantity is the doubly-phase-resolved mean, which represents the average value of  $\zeta$  at a particular phase angle combination, viz.

$$\bar{\zeta}^{ah}(x, y, \phi_a, \phi_h) = \bar{\zeta}(x, y) + \zeta^{ah}(x, y, \phi_a, \phi_h) \quad (4)$$

Additionally, it is useful to define the local oscillation at a given location and  $\phi_h$ , relative to the average over the acoustic cycle at that location and  $\phi_h$ , viz.

$$\zeta^a(x, y, \phi_a, \phi_h) = \bar{\zeta}^{ah}(x, y, \phi_a, \phi_h) - \frac{1}{N_p} \sum_{\phi_a=1}^{N_p} \bar{\zeta}^{ah}(x, y, \phi_a, \phi_h) \quad (5)$$

In addition to velocity field analysis, doubly-phase-resolved analysis also can be used to quantify the oscillatory behavior of the flame. To do so, a statistical representation of the flame is required. For the premixed flames studied here, the turbulence intensity was such that the flames are in the corrugated flamelet regime. Under such conditions, chemical reactions occur in thin layers and the local heat release rate is the product of the flame surface area and the reaction rate per unit area. Lean methane-air flames have heat release rates per unit area that are relatively independent of the local flow-field (i.e. Markstein numbers near

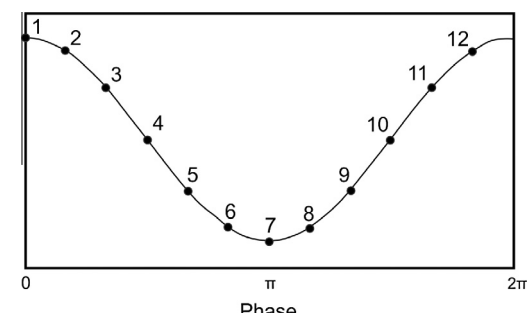


**Fig. 6.** Definition of phase numbers used for doubly-phase-resolved analysis.

zero). Hence, to first order, the volumetric heat release rate is proportional to the flame surface area per unit volume, i.e. the flame surface density (FSD),  $\Sigma$ . The oscillatory flame behavior can then be quantified by double-phase-resolution of  $\Sigma$ .

To calculate  $\Sigma$ , the instantaneous reaction layer topology was calculated from the magnitude and gradient of the OH PLIF images using the algorithm described in Ref. [32]. The measurement domain was then divided into  $1.7 \text{ mm} \times 1.7 \text{ mm}$  cells and the flame length per unit area determined. Doubly-phase-resolved flame-surface-density fields were then calculated as the mean flame surface length per unit area at each combination of phase angles.

This is demonstrated in Fig. 7. Figures 7a and b show two typical instantaneous OH PLIF measurements taken at the maximum of the pressure cycle ( $\phi_a = 1$ ) but at two different HVC phases ( $\phi_h = 1$  and 7). Figures 7c and d show the mean doubly-phase-resolved flame surface density fields at these phase combinations

(viz.  $\bar{\Sigma}_y^{ah}(x, y, \phi_a = 1, \phi_h = 1 \text{ or } 7)$ ). The HVC's intersection with the measurement plane is shown as a swirling strength iso-contour in all figures. Clearly, the statistical fields resemble the instantaneous fields and depend strongly on  $\phi_h$ . These images demonstrate the need to resolve the HVC phase in addition to the acoustic phase to understand the thermo-acoustic coupling in such systems.

It is noted that doubly-phase-resolved analysis allows visualization of oscillatory processes in 3D [31]. That is, statistics compiled at a particular  $\phi_h$  represent processes occurring at a particular azimuthal location along the HVC helix. Such statistics can be compiled either at each particular  $\phi_a$  or of average processes integrated over the acoustic cycle. For example, at  $\phi_a = 1$ , the doubly-phase-resolved planar fields of  $\bar{u}_y^{ah}(x, y, \phi_a = 1, \phi_h = 1 \dots 12)$  represent 12 different slices of the mean 3-D axial velocity field at the maximum of the pressure cycle. Connecting these azimuthal slices based on their angular position in the HVC cycle allows useful visualization of 3D processes.

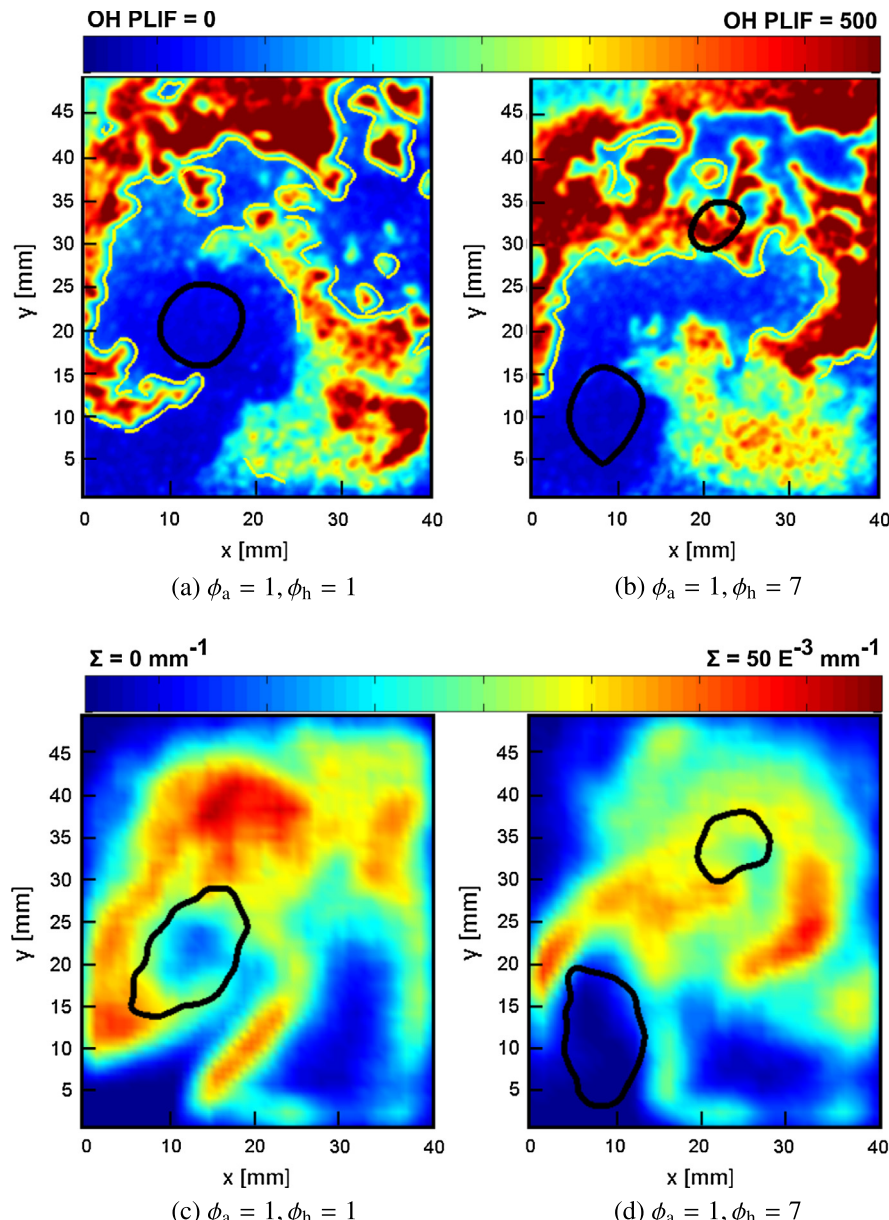


**Fig. 7.** Typical instantaneous OH PLIF intensity fields ((a) and (b)) taken at the acoustic phase of highest pressure ( $\phi_a = 1$ ), and different locations along the HVC ( $\phi_h = 1$  and 7). These instantaneous fields resemble the statistical flame surface density fields of (c) and (d), taken at the same phase combination, respectively. In each figure, the HVC is shown by black iso-contours of swirl strength at 30% of the maximum swirl strength value.

### 3.3. Statistical solution of the Rayleigh integral

Direct solution of Eq. (1) requires knowledge of the 3D pressure and heat release dynamics throughout the combustor volume. For the burner studied here, the pressure oscillations were essentially spatially uniform throughout the combustion chamber volume due to the Helmholtz resonance of the system. The volumetric heat release rate was taken to be proportional to the flame surface density. The thermo-acoustic energy transfer distribution is then characterized by:

$$\theta(\vec{x}) \sim \int_t p'(t) \Sigma'(\vec{x}, t) dt \quad (6)$$

For configurations where heat release oscillations occur in radially symmetric patterns (i.e. with periodic shedding of toroidal vortices), planar measurements and Eq. (6) can be used to gain insight into the thermo-acoustic velocity coupling. However, for systems with HVCs, wherein heat release oscillations occur in complex 3D patterns that depend on the HVC azimuthal position, Eq. (6) cannot directly reveal the velocity coupling.

It was shown in Ref. [31] that doubly-phase-resolved analysis can be used to better understand the velocity coupling in such systems. In this case, the Rayleigh integral is taken over the thermo-acoustic cycle (i.e. over the  $\phi_a$  oscillation) at each azimuthal position along the HVC (i.e.  $\phi_h$ ). The resultant coupling distribution is given by:

$$\psi(x, y, \phi_h) = \frac{1}{N_p} \sum_{\phi_a=1}^{N_p} p^a(\phi_a) \Sigma^a(x, y, \phi_a, \phi_h) \quad (7)$$

and the total thermo-acoustic coupling is represented by

$$\Psi = \sum_{\phi_h=1}^{N_p} \int_x \int_y \psi(x, y, \phi_h) dx dy. \quad (8)$$

The relationship between the total thermo-acoustic energy transfer computed using Eq. (8) and the measured pressure oscillation amplitude is shown in Fig. 8. Louder cases are associated with greater thermo-acoustic energy transfer, clearly demonstrating that  $\Psi$  is a good representation of thermo-acoustic coupling. Moreover, Fig. 9 shows the evolution of the total FSD fluctuation

$$\{\Sigma^a(\phi_a)\} = \frac{1}{N_p} \sum_{\phi_h=1}^{N_p} \int_{x=0}^{x_{\max}} \int_{y=0}^{y_{\max}} \Sigma^a(x, y, \phi_a, \phi_h) dx dy \quad (9)$$

over the thermo-acoustic cycle for a quite case (Case 3), an intermediate case (Case 5b), and the loudest case (Case 6). Also shown is a representative pressure signal that indicates the phase in the acoustic cycle. As can be seen, the phase-shift between the acoustics and

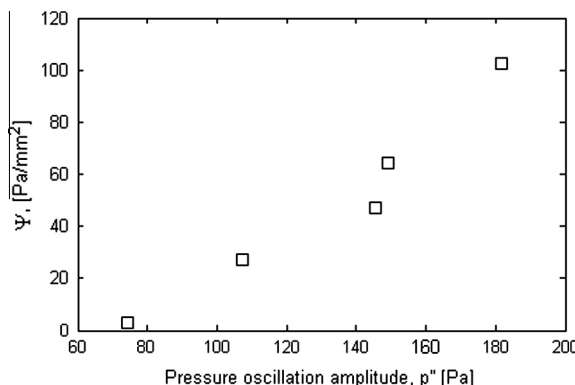


Fig. 8. Thermo-acoustic energy transfer versus RMS pressure oscillation amplitude.

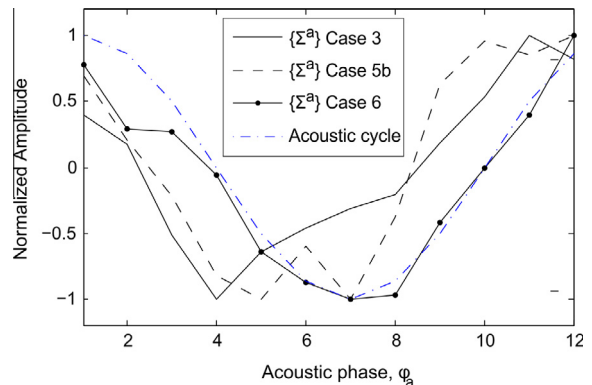


Fig. 9. Fluctuations of the spatially integrated flame surface density ( $\{\Sigma^a\}$ ) over the acoustic cycle for the Cases 3, 5b, and 6. The acoustic cycle is shown as a dash-dotted line for phase referencing.

FSD oscillations decreased with increasing pressure amplitude. For example,  $\{\Sigma^a\}$  for Case 3 reached a minimum at  $\phi_a = 4$ , whereas the pressure reached a minimum at  $\phi_a = 7$  (by definition, see Section 3.2). Hence, for the 12-segment phase decomposition performed in this analysis,  $\{\Sigma^a\}$  of Case 3 was approximately 90° out-of-phase with the pressure. Conversely,  $\{\Sigma^a\}$  for Case 6 was perfectly in-phase with the acoustic cycle. These phase relationships will be discussed more in Section 4.3. However, it can be seen that the thermo-acoustic energy-transfer analysis produces results that are consistent with the observed oscillation amplitudes.

However, neither  $\Psi$  nor  $\{\Sigma^a\}$  provide insight into the underlying processes responsible for the thermo-acoustic energy transfer, let alone where along the HVC is the energy transfer more prominent. To this end, it is more useful to look at the distribution of the volumetric thermo-acoustic energy transfer,  $\psi$ . The remainder of this paper focuses on understanding the distribution  $\psi$  and the controlling velocity-coupling mechanisms.

## 4. Results and analysis

### 4.1. Thermo-acoustic energy transfer ( $\psi$ ) distributions

Figure 10 shows  $\psi$  for the three characteristic cases in Fig. 9 (Cases 3, 5b, and 6). Regions of high positive and negative  $\psi$  are shown by green and blue isosurfaces respectively, while the helical vortex is displayed with a red vorticity isosurface. These figures can be thought of as being in a frame that is rotating with the HVC and demonstrate that each case exhibits some similar  $\psi$  features with different distributions, namely

1. An inner coupling region (ICR) composed of negative and positive  $\psi$  zones, denoted by 1 and 2 respectively, that are bound by the HVC.
2. An outer coupling region (OCR), denoted by 3, that surrounds the HVC.

For the quieter cases, the ICR contained mostly positive  $\psi$ , whereas the OCR contained mostly negative  $\psi$ . For the louder cases, the net  $\psi$  in the ICR became approximately zero, whereas the OCR changed from negative to positive  $\psi$ . Hence, the OCR is responsible for most of the positive-thermo-acoustic coupling in the louder flames. Furthermore, at a given azimuthal position,  $\psi$  in the ICR and OCR had opposite signs. Comparing the quite and loud cases, the high magnitude coupling in the OCR changed in position relative to the HVC by approximately 180°. Recall from the Rayleigh integral (Eq. (1)) that regions of positive and negative  $\psi$  indicate regions in which the heat release oscillations were

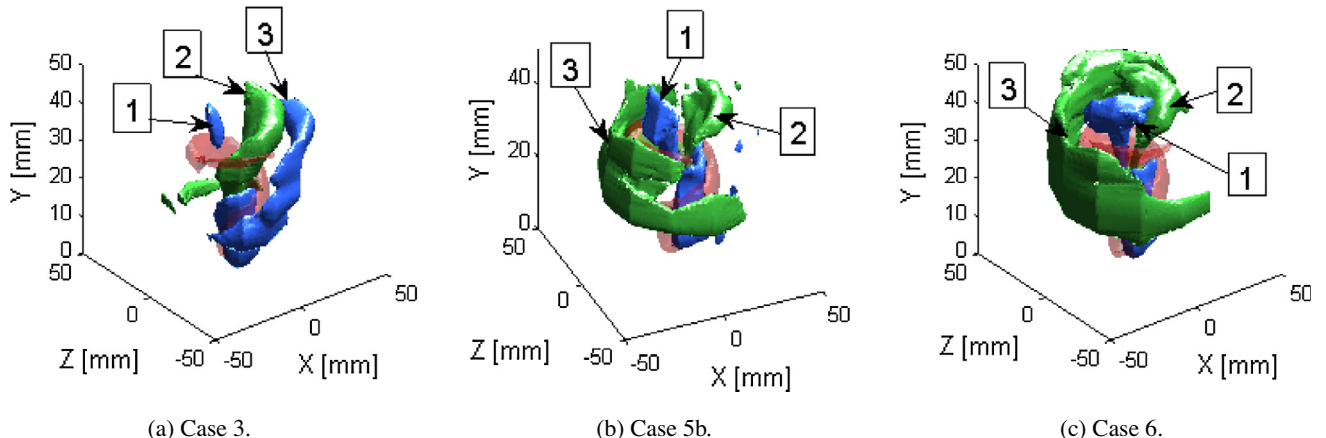


**Fig. 10.** Isosurfaces of volumetric thermo-acoustic energy transfer ( $\psi$ ) for characteristic cases. The red isosurface is vorticity at  $5000 \text{ s}^{-1}$ . Regions 1 and 2 are negative and positive  $\psi$  in the ICR, respectively. Region 3 is the OCR. (For interpretation of the references to color in this figure legend, the reader is referred to the web version of this article.)

in- and out-of-phase with the acoustics, respectively. Hence, changes in the sign of  $\psi$  indicate a change in phase of the local heat release oscillations with respect to the pressure oscillations.

#### 4.2. Flow-flame interactions causing $\psi$ distributions

With an essentially spatially uniform pressure field in the combustion chamber, Eq. (7) shows that the spatial distribution of  $\psi$  is set by the spatial and phase (relative to the pressure) distribution of  $\Sigma^a$ . Flame surface density oscillations are related to periodic generation and destruction of flame surface, which can be caused by local flame extinction, flame stretch/corrugation, or ignition of unburnt reactants. The influence of periodic local flame extinction on  $\psi$  was quantified by computing the statistical area of flame holes from the OH PLIF at each phase angle combination (see Appendix A). However, no significant variation was found in the number or area of flame holes over the thermo-acoustic cycle. The observed FSD oscillations therefore were due to flow-flame interactions periodically altering the amount of contiguous flame surface area. Since the HVC was the dominant flow-structure in the studied flames, understanding its interaction with the flame

is critical. The following discussion demonstrates the flow–flame interactions for the loudest and quietest flames studied.

#### 4.2.1. Loudest flame – Case 6

**Figure 11** shows several aspects of doubly-phase-resolved flow and flame over the thermo-acoustic cycle at  $\phi_h = 1$  for Case 6. This value of  $\phi_h$  shows several representative features of the flow-flame interactions. The location at which the HVC intersected the measurement plane is shown by the thick line at a swirling strength iso-contour taken at 30% of the maximum value. Also shown are fluctuations of various quantities relative to the average over the acoustic cycle at this  $\phi_h$ . The background shows  $\Sigma^a$  (the FSD fluctuation field) at each  $\phi_a$ , which indicates how the heat release moved around the combustor over the thermo-acoustic cycle. The arrows show the velocity field fluctuation ( $\vec{u}^a$ ) at each  $\phi_a$  and the flyouts show the vorticity associated with the  $\vec{u}^a$  field ( $\omega_x^a$ ). The velocity fluctuations were computed from the doubly-phase-resolved quantities in accordance to Eq. (5). Note that vorticity is used here instead of swirling strength. While swirling strength is a more robust means of identifying vortices, it cannot identify the sense of rotation of a vortex. This sense of rotation is important in the analysis that follows, and therefore vorticity is used henceforth.

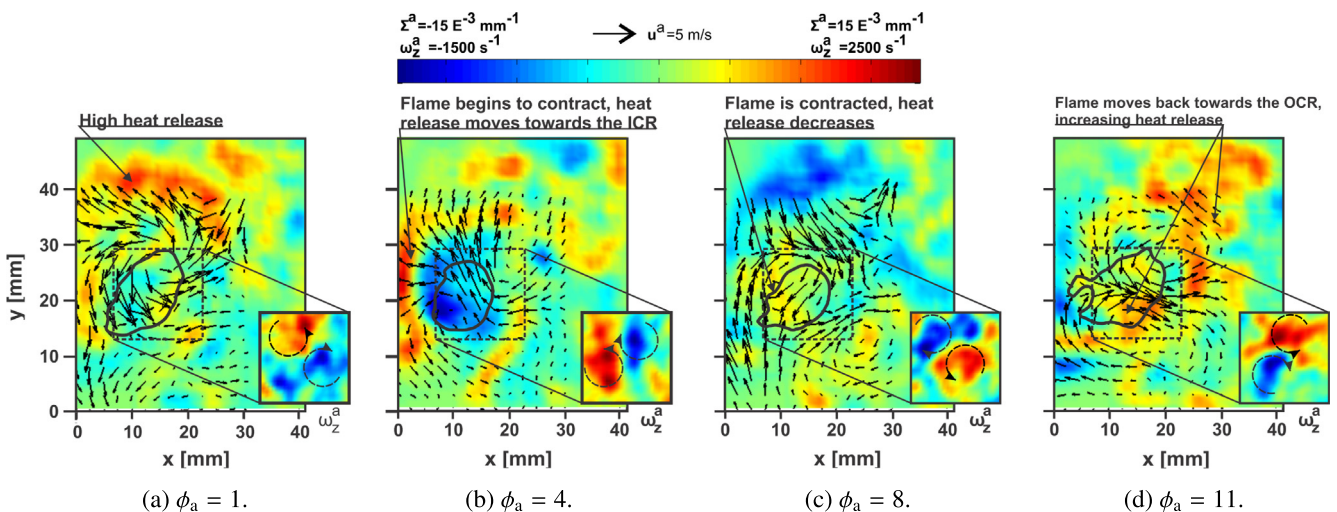


**Fig. 11.** Evolution of flame surface density fluctuations ( $\Sigma^3$ ) and velocity fluctuations ( $\mathbf{u}^3$ ) over the acoustic cycle at  $\phi_h = 1$  for Case 6. The HVC is shown by black iso-contours of swirl strength at 30% of the maximum swirl strength value. The fly-outs show  $\omega_z^3$  in the vicinity of the HVC.

Firstly, it can be seen that the heat release distribution moved around the combustor over the thermo-acoustic cycle. Starting from  $\phi_a = 1$ , the region of positive  $\Sigma^a$  moved counter-clockwise. As it did so, the total flame surface density initially decreased until  $\phi_a = 8$ , after which it increased again until  $\phi_a = 11$ . The heat-release decrease was associated with contraction of the flame towards the nozzle (the ICR), whereas the heat-release increase was associated with combustion towards the periphery of the burner (the OCR). The region of high heat-release then moved towards the axis at  $\phi_a = 1$ , after which the process repeated. Essentially, the heat release oscillations are associated with periodic transport of the flame and/or hot products to ignite fresh reactants in the OCR, followed by flame transport towards the ICR and contraction.

The flame motion is associated with oscillations in the velocity field, as shown by the vector arrows. It was found that these oscillations are well visualized by the vorticity field associated with the velocity fluctuations, shown in the flyouts of Fig. 11. Essentially, over the thermo-acoustic cycle, the flow-field oscillated in a manner that transported flame surface around the combustor. For example, at  $\phi_a = 11$ , the velocity oscillations were such that reactants were transported towards the combustor periphery. The flow-field associated with this oscillation appeared as a pair of counter-rotating  $\omega_z^a$  structures. Over the thermo-acoustic cycle, the velocity field changed such that the oscillations moved the flame in a circular motion. This was associated with a rotation in the orientations of the  $\omega_z^a$  structures. Eventually, the velocity oscillations transported the flame towards the burner centerline and reduced the total amount of combustion. The critical velocity oscillations occurred around the region where the HVC intersected the measurement plane. Hence, it is clear the HVC is critical in setting the thermo-acoustically coupled flame dynamics.

This also is apparent at values of  $\phi_h$  where the HVC intersected the measurement plane at two locations. However, two regions of important flow oscillations, visualized as two pairs of  $\omega_z^a$  structures, occurred at the two HVC locations. Figure 12 shows the same quantities as the sequence of Fig. 11, but for  $\phi_h = 7$ . At the acoustic phase of highest pressure ( $\phi_a = 1$ ), the  $\omega_z^a$  structures near the top and bottom HVC intersections were rotated by approximately  $180^\circ$  relative to each other, such that the flame was pushed into the OCR near the top of the measurement region and towards the burner axis near the bottom. This resulted in the creation of positive  $\Sigma^a$  in these areas. At the acoustic phase of lowest pressure ( $\phi_a = 7$ ), the flow field changed such that the flame was pushed in the opposite directions to those occurring at  $\phi_a = 1$ . This is visualized by both  $\omega_z^a$  structures rotating by  $180^\circ$ . At the top of the measurement region, this led to negative  $\Sigma^a$  in the OCR and positive  $\Sigma^a$  in the ICR. On the other hand, the flame in the vicinity of the nozzle moved radially outward, creating positive  $\Sigma^a$ . Once again, it is clear that the important velocity oscillations are associated with some dynamics of the HVC.

#### 4.2.2. Quietest case – Case 3

The general behavior of the flow–flame interactions in the quietest case (Case 3) were very similar to those of the loudest case; the phase shift relative to the acoustics was the primary difference. To highlight these similarities and differences, the analogous image sequence to Fig. 11 is shown in Fig. 13 for Case 3. For a representative comparison,  $\phi_h$  was chosen so that the HVC was at the same axial location as the one in Fig. 11;  $\phi_h = 2$  is shown instead of  $\phi_h = 1$ .

As for Case 6, velocity fluctuations occurred that moved the flame around the combustors, which are well visualized by the rotation of the  $\omega_z^a$  structures. These velocity fluctuations caused flame transport between the burner periphery (OCR) and axis (ICR). The most significant difference between the Case 3 and Case

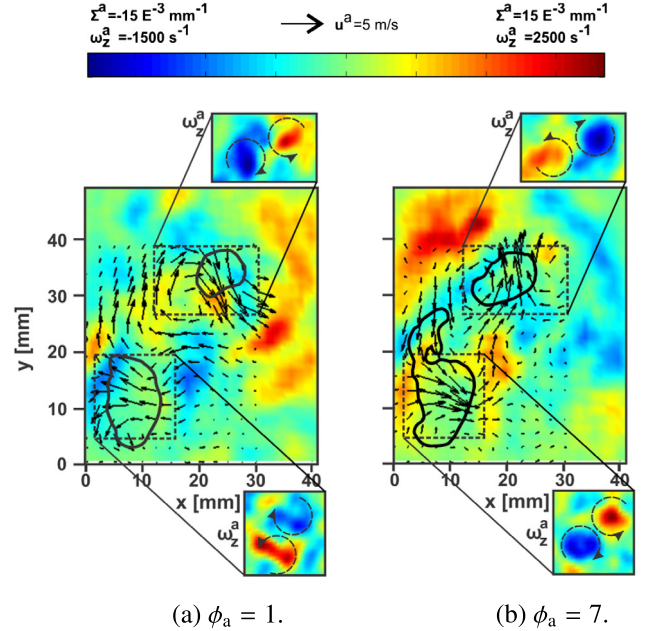


**Fig. 12.** Evolution of flame surface density fluctuations ( $\Sigma^a$ ) over the acoustic cycle and velocity fluctuations ( $\mathbf{u}^a$ ) at  $\phi_h = 7$  for Case 6. The HVC is shown by black iso-contours of swirl strength at 30% of the maximum swirl strength value. The fly-outs show  $\omega_z^a$  in the vicinity of the HVC.

6 was a notable shift in the orientation of the velocity oscillations at a given  $\phi_a$ . For example, the  $\omega_z^a$  structures for Case 3 had the same orientation at  $\phi_a = 1$  as occurred at  $\phi_a = 11$  for Case 6. Hence, the mechanism setting the flame dynamics was shifted in phase and so were the resultant heat release oscillations.

From the above discussion, it is apparent that the mechanisms and dynamics of heat release oscillations were the same in the quietest and loudest cases. The increase in thermo-acoustic energy transfer from the quietest to the loudest case therefore does not result from a change in the fundamental nature of the flow–flame interactions, but rather from a change in the phase (relative to the acoustics) at which these interactions occur. Since the heat release dynamics were associated with velocity fluctuations in the vicinity of the HVC, a thorough understanding of the flow-field in this region is required.

#### 4.2.3. Origin of the velocity fluctuation pattern

The origin of the velocity field fluctuations was found to be largely driven by changes in the shape of the HVC over the thermo-acoustic cycle. That is, at each HVC phase, the position at which the HVC intersected the measurement plane changed over the thermo-acoustic cycle. This is illustrated in the cartoon of Fig. 14, which shows the red HVC's intersection with the measurement plane. A white cross marks the swirling-strength weighted doubly-phase-resolved centroid ( $\bar{x}_c^{ah}$ ,  $\bar{y}_c^{ah}$ ) of each HVC intersection, which were computed over the region around the local swirling-strength peaks corresponding to values greater than half the local maximum. The deformation of the HVC in Fig. 14 is exaggerated for clarity, and the actual vortex intersection displacements calculated from  $\bar{x}_c^{ah}$  and  $\bar{y}_c^{ah}$  are shown in Fig. 15 for different HVC phases.

To understand how the HVC deformation resulted in the observed fluctuations in the velocity field, it is useful to consider a simple unidirectional deformation of the HVC. As the HVC moves, for example, from left to right, the region of high vorticity also is displaced. Hence, negative and positive  $\omega_z^a$  oscillations would occur to the left and right of the mean HVC position, respectively. The previously noted rotation of the  $\omega_z^a$  structures therefore was a

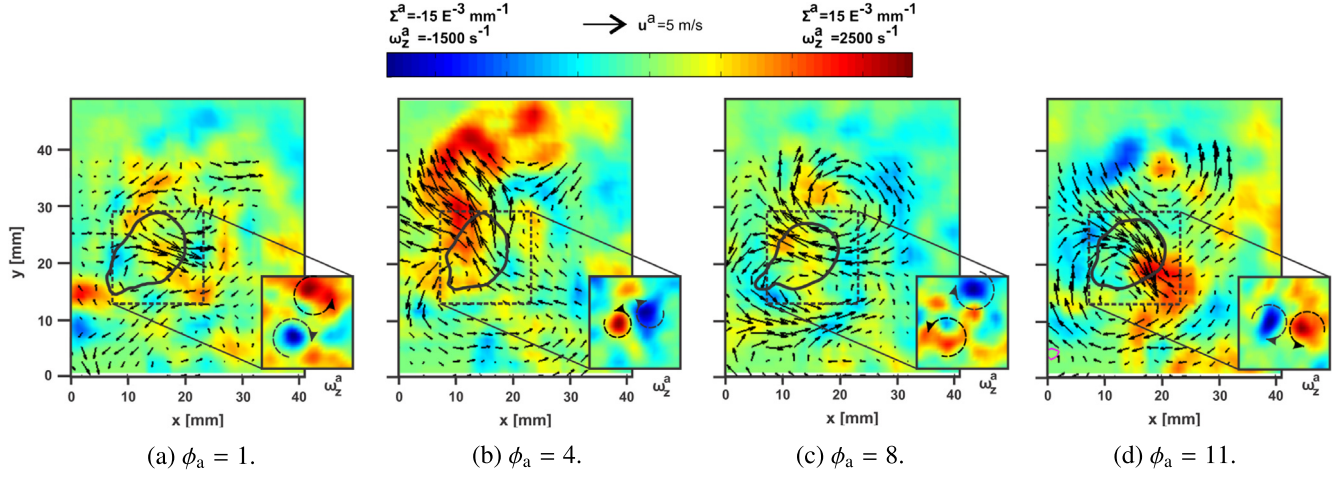


**Fig. 13.** Evolution of flame surface density fluctuations ( $\Sigma^a$ ) over the acoustic cycle and velocity fluctuations ( $u^a$ ) at  $\phi_h = 2$  for Case 3. The HVC is shown by black iso-contours of swirl strength at 30% of the maximum swirl strength value. The fly-outs show  $\omega_z^a$  in the vicinity of the HVC.

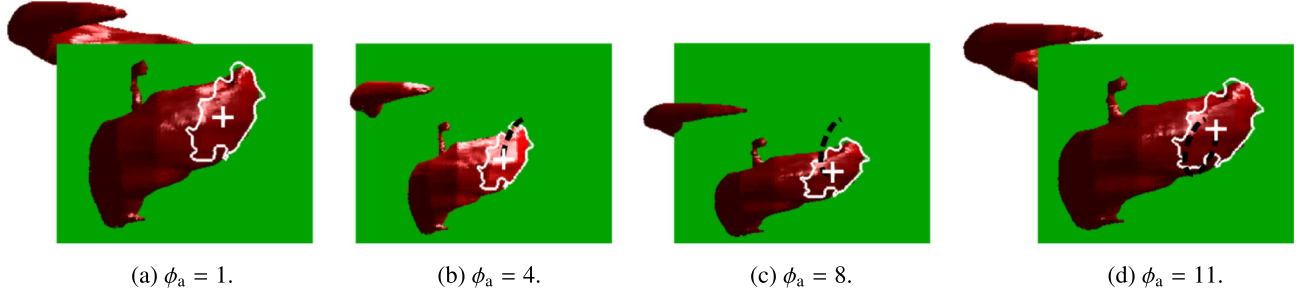


**Fig. 14.** Illustration of the HVC's deformation over the acoustic cycle. The HVC is shown as a red vorticity isosurface ( $\omega_z = 5000 \text{ s}^{-1}$ ) and the PIV measurement plane is shown in green. The intersection of the HVC and the measurement plane is shown in white, with a white cross marking the location of the swirling-strength weighted centroid of the vortex intersection. The elliptical trajectory of the HVC intersection is depicted by a dashed black line, tracing the location of the vortex intersection's centroid over the acoustic cycle. (For interpretation of the references to color in this figure legend, the reader is referred to the web version of this article.)

result of the elliptical trajectory of the HVC intersection, observed as a phase lag between the axial and radial displacements in Fig. 15.

The presence of the HVC therefore affects the flame in two main ways. Firstly, it affects the ‘zero-mode’ of the flame, i.e. the mean heat release distribution. Secondly, the flow–flame interactions associated with deformation of the HVC at the thermo-acoustic frequency couples the mean heat release distribution with the acoustic oscillations (the mechanism of this deformation will be discussed below). The change in total heat release over the thermo-acoustic cycle was not due to the HVC’s precession around the burner, which occurred at a different frequency, but rather by its axial deformation at the thermo-acoustic frequency.

#### 4.2.4. Origin of the HVC deformation

The formation and geometry of the HVC is linked to the swirl-number,  $S$ , which is defined as the ratio of azimuthal to axial momentum flux. It previously has been observed that  $S$ -waves in thermo-acoustically oscillating swirl-flames can be linked to periodic axial velocity waves, which are caused by the changing pressure difference between the combustion chamber and plenum over the thermo-acoustic cycle [55]. Axial velocity and swirl number fluctuations can be related by performing a Reynold’s decomposition, which yields

$$\frac{S'}{\bar{S}} \sim -\frac{u'_y}{\bar{u}_y} \quad (10)$$

From this relationship, it is clear that  $S'$  and  $u'_y$  should be negatively correlated.

The propagation of any wave can be observed by integrating the property of interest across the burner width at every axial position, *viz.*

$$\langle \xi(y, \phi_a, \phi_h) \rangle = \frac{1}{x_{max}} \int_0^{x_{max}} \xi(x, y, \phi_a, \phi_h) dx \quad (11)$$

The cross-section integrated axial velocity fluctuations  $\langle u_y^a \rangle$  are shown in Fig. 16 for different acoustic phases of Case 6, clearly showing the convecting axial velocity wave. Figure 17 shows  $\langle u_y^a \rangle$  and  $\langle S^a \rangle$  at  $\phi_a = 1$ , which demonstrates the expected negative correlation. Such swirl number waves were also noticed by Palies et al. [55,56], and are thought to affect the shape of the HVC through a displacement of the central recirculation zone.

Palies et al. also observed that the swirl wave was convected by the mean flow. To verify this in the present data set,  $\langle S^a \rangle$  was plotted versus  $y$  and  $\phi_a$ . This is shown in Fig. 18 for Case 6, with the colormap indicating  $\langle S^a \rangle$ , and a black line showing a linear fit to the maxima. The convective speed of the wave was calculated from

$$v_S = \Delta y N_p f_{ac} / \Delta \phi_a \quad (12)$$

where the  $N_p f_{ac}$  is included to convert from phase-space to time. This speed is compared to the mean inlet flow velocity in Table 2, from which it can be seen that the swirl wave did indeed propagate at the mean flow velocity, with a maximum disagreement of 9%.

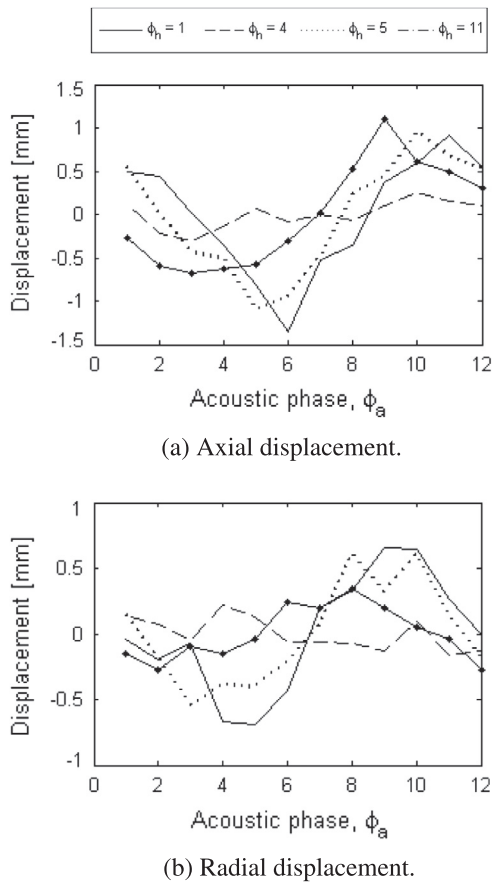


**Fig. 15.** Axial and radial displacement of the HVC centroid for Case 6 over the acoustic cycle.

#### 4.3. Phase relationships

From the discussion above, it is clear that the velocity coupling mechanism was similar for all cases, while the phase at which the particular flow and combustion dynamics occurred (relative to the acoustics) was a function of the combustor conditions and  $\phi_h$ . This phase depends on the feedback mechanism that couples the acoustics and heat release, which can be summarized as follows:

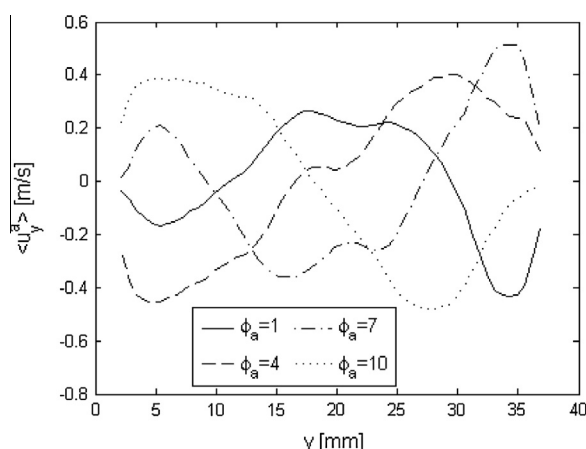


**Fig. 16.** Axial distribution of  $\langle u_y^a \rangle(\phi_a)$  versus axial location at different acoustic phases.

1. A pressure oscillation in the combustion chamber results in a *S*-wave (associated with an axial velocity wave), that convects from the combustor nozzle at the axial flow speed.
2. The *S* wave causes changes in the shape of the vortex-breakdown-related HVC, which is associated with velocity oscillations that can be visualized by rotating  $\omega_z^a$  structures.
3. These velocity oscillations cause periodic motion of the flame between the periphery (OCR) and centerline (ICR), resulting in periodic heat release oscillations.

Hence, the phase of the heat release oscillations relative to the acoustics ( $\phi_{\{\Sigma^a\}-a}$ ) can be expressed as a function of three distinct phase lags, one associated with each process:

1. The phase lag between the swirl-wave reaching the nozzle dump-plane and the combustion chamber acoustics  $\phi_{\langle S^a \rangle-a}$ . It is noted that the swirl-wave actually initiates in the swirl-nozzle itself and propagates to the dump plane. However, the analysis below is based on the phase of the velocity (and hence swirl) oscillations at the nozzle/chamber interface.
2. The phase lag between the wave production and its interaction with the HVC.
3. The phase lag between the HVC-related flow oscillations and the flame response.

The latter two processes are actually continuous processes involving the swirl number wave interacting with the spatially distributed HVC and the HVC interacting with the spatially distributed flame. As a consequence, the quantity of interest is the net phase lag between the generation of the swirl number wave and the mean FSD oscillation. Hence, this study will treat the latter two as a single phase lag, denoted  $\phi_{\{\Sigma^a\}-\langle S^a \rangle}$ . This quantity accounts for the global effect of the spatially variant swirl number oscillations and the heat release rate. The phase of  $\{\Sigma^a\}$  relative to the acoustic cycle therefore may be expressed as

$$\phi_{\{\Sigma^a\}-a} = \phi_{\langle S^a \rangle-a} + \phi_{\{\Sigma^a\}-\langle S^a \rangle}, \quad (13)$$

The overall phase lag between the heat release and pressure oscillations ( $\phi_{\{\Sigma^a\}-a}$ ) can be assessed from curves such as those in Fig. 9. Similar curves were constructed for all cases, as well as for the phase lag between the swirl wave and acoustics ( $\langle S^a \rangle(y=0, \phi_a)$ ). Quantification of the phases then was performed by fitting a cosinusoid to these curves. The results are plotted versus the RMS pressure amplitude in Fig. 19a. Changes in the phase of the heat release oscillations were well correlated with changes in the phase of the swirl-number wave, highlighting the importance of the swirl-number wave on setting the heat release oscillations. It

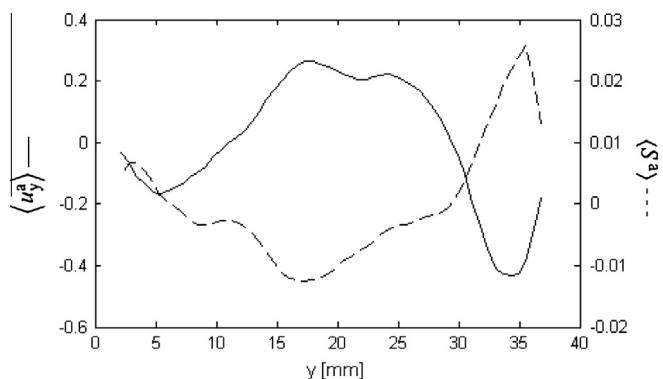


**Fig. 17.** Axial distribution of  $\langle u_y^a \rangle$  and  $\langle S^a \rangle$  at  $\phi_a=1$  for case 6. Local swirl number fluctuations are imparted by axial velocity fluctuations, with a  $180^\circ$  phase shift in the two waves resulting from Eq. (10).

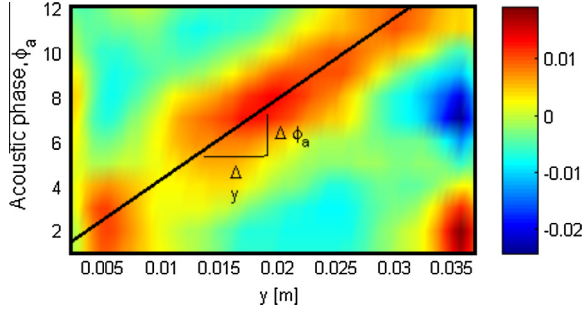


**Fig. 18.** Swirl fluctuation versus axial position and the acoustic cycle. The convective speed of the  $\langle S^a \rangle$  wave was found by fitting a line through the  $\langle S^a \rangle$  weighted domain. The speed can be evaluated by taking the reciprocal of the line's slope.

**Table 2**

Comparison of the mean inlet flow velocity and the convective speed of the swirl wave.

Case	$\bar{u}_y$ (m/s)	$v_s$ (m/s)	$\frac{ \bar{u}_y - v_s }{\bar{u}_y}$ (%)
3	8.0	8.7	9
4	9.2	9.6	4
5b	11.1	11.3	2
5c	11.3	11.3	0
6	12.9	13.4	4

is noted that the point that deviates slightly from the trend was a high-power case, which resulted in relatively high oscillation amplitudes despite a moderate  $(\phi_{\{\Sigma^a\}-a})$ .

It now remains to explain the mechanisms setting  $\phi_{\{S^a\}(y=0,\phi_a)}$  and the relative phase between the swirl wave and the flame response  $(\phi_{\{\Sigma^a\}-\langle S^a \rangle})$ . The former will be treated in Section 4.3.1 below. The phase relationship between the generation of the swirl wave and  $\{\Sigma^a\}$  was computed from Eq. (13), and is shown versus the RMS pressure amplitude in Fig. 19b. As indicated above, this relationship encompasses both the time required for the swirl wave to affect the flow and for the flow to affect the flame. Hence, it accounts for both the convection of the wave to the spatially distributed HVC and flame, as well as the flame response. Table 2 showed that wave convected at the mean axial flow speed. Figure 19c shows  $\phi_{\{\Sigma^a\}-\langle S^a \rangle}$  vs. the wave speed and clearly indicates that, as this speed increased, it took less time for the swirl number oscillations at the nozzle exit plane to travel downstream and affect the flow/flame. Deviations from a linear profile are attributed to differences in the flame shape between cases.

#### 4.3.1. Helmholtz-resonator model for $\phi_{\{S^a\}-a}$

We now seek an analytic description of the phase between the generation of the swirl number wave at  $y = 0$  and the combustor acoustics. The  $S$  wave is related to the axial velocity wave by Eq. (10), which in doubly-phase-resolved notation is

$$\langle S^a(y, \phi_a) \rangle = -\bar{S} \frac{\langle u_y^a(y, \phi_a) \rangle}{\bar{u}_y} \quad (14)$$

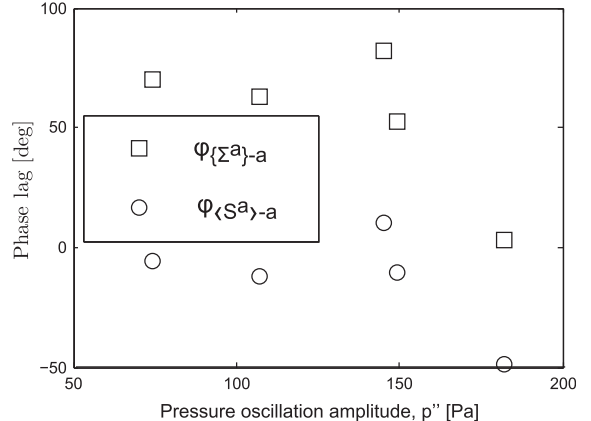
The mean swirl number ( $\bar{S}$ ) and flow speed ( $\bar{u}_y$ ) may be estimated from the mass flow rate of reactants and the geometry of the burner. Determining the phase of the  $S$ -wave therefore requires determining the phase of the axial velocity wave. Recalling that the system behaved like a multi-chamber Helmholtz resonator, the acoustically-coupled bulk-flow dynamics can be modeled as a spring-mass-damper system [57].

In such a model the burner geometry is represented as a sequence of cylindrical chambers that preserve the length, cross-sectional area, and volume of the different burner components,

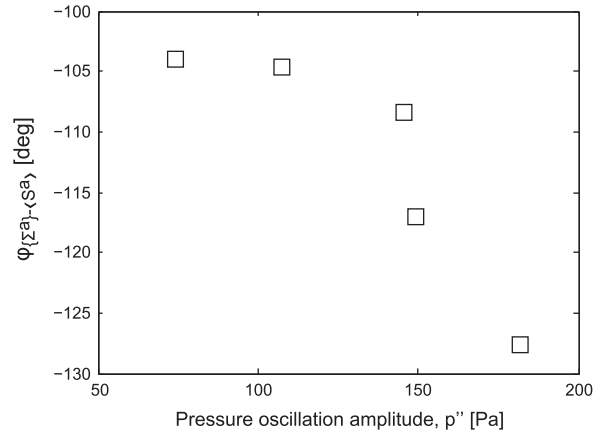
as illustrated in Fig. 20. The response of this simplified geometry can then be expressed analytically as a function of the chamber pressure oscillation amplitude and frequency viz.

$$\phi_{\langle S^a \rangle-a} = \tan^{-1} \left( \frac{\Im(U_y)}{\Re(U_y)} \right) + \pi, \quad (15)$$

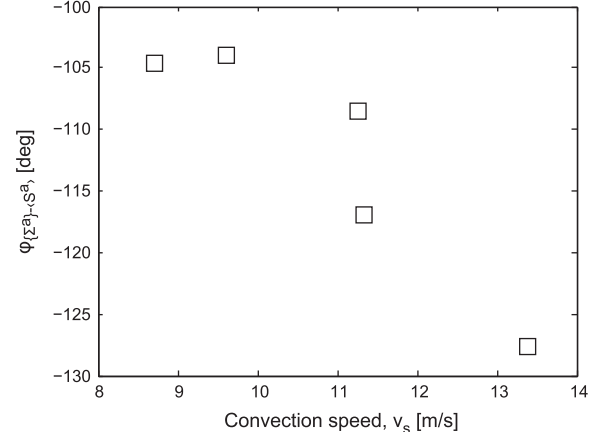
where



(a) Phase lag of  $\{\Sigma^a\}$  and  $\langle S^a \rangle$  ( $y = 0, \phi_a$ ) relative to the acoustic oscillation.



(b) Phase lag between  $\langle S^a \rangle$  ( $y = 0, \phi_a$ ) and  $\{\Sigma^a\}$ .



(c)  $\langle S^a \rangle$  ( $y = 0, \phi_a$ ) and  $\{\Sigma^a\}$  as a function of the convection speed of the swirling strength wave.

**Fig. 19.** Phase relationship between the acoustic cycle,  $\{\Sigma^a\}$  and  $\langle S^a \rangle$  ( $y = 0, \phi_a$ ), and their relationship with the convective speed of the swirling strength wave.

$$U_y = \frac{i \omega A_s p''}{m_s \omega^2 - b \omega i - k A_s}. \quad (16)$$

In the above equations,  $U_y$  is the axial velocity wave,  $A_s$  is the cross section area of the swirller,  $m_s$  is the mass of fluid in the swirller,  $\omega$  and  $p''$  are the angular frequency and amplitude of the chamber pressure fluctuations,  $b$  is a damping constant, and  $k$  is a stiffness constant. While the stiffness ( $k$ ), damping ( $c$ ), and inertial ( $m_s$ ) constants are based on physical quantities, and can potentially be derived from information about the combustor geometry, here they were computed by non-linear least squares curve fitting of acoustics simulations by Im [52]. To validate the computed values,  $\phi_{(S)-a}$  was calculated from Eq. (15) and compared to the experimental values of Fig. 19a. This comparison is shown in Fig. 21, in which

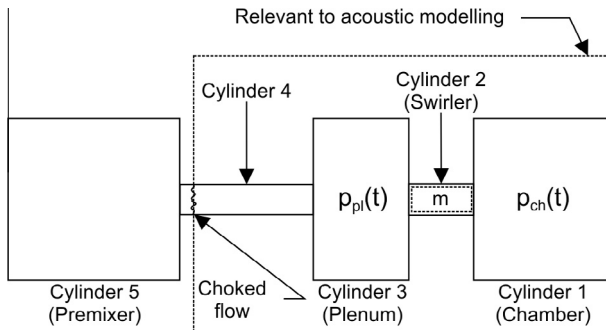


**Fig. 20.** Simplified representation of the model combustor using a network of cylinders.

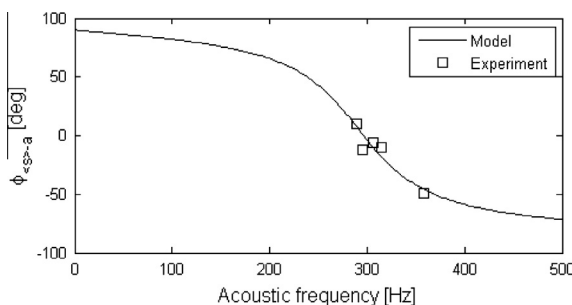


**Fig. 21.** Phase lag of the swirl oscillations relative to the combustion chamber pressure oscillations as a function of acoustic forcing frequency. The Helmholtz resonator model (solid line) and experimental data (square markers) show good agreement, allowing for simple prediction of the phase of the swirl wave or swirl number wave.

good agreement between the model and the experimental data shows that Helmholtz resonator modeling of the combustor is a useful tool for accurate prediction of the phase lag between the swirl number wave and the chamber acoustics.

## 5. Conclusion

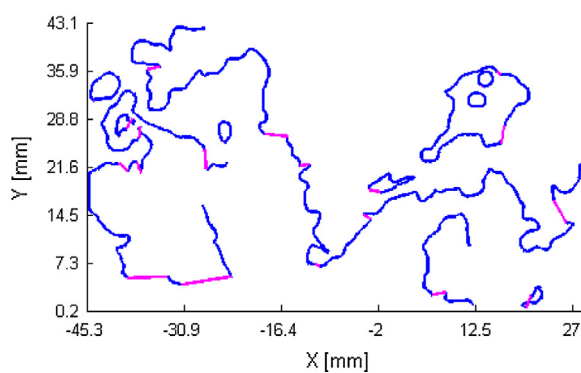
Thermo-acoustic coupling in a swirl-stabilized gas turbine combustor burning lean premixed methane-air flames was investigated through analysis of data from high-repetition-rate laser diagnostics. Five different operating conditions were discussed, all of which contained a helical vortex core as a dominant flow feature. The flow features were resolved as a function of both the acoustic phase, and the azimuthal position along the helical vortex core, allowing 3-D reconstruction of statistical measurements.

In all cases, thermo-acoustic energy transfer was caused by a deformation of the helical vortex, which displaced the acoustically-resolved mean position of the flame front via the associated velocity fluctuations. The net heat release oscillations became increasingly in phase with the acoustic cycle for cases with increasing thermo-acoustic oscillation amplitude, thereby driving the oscillations. The pressure oscillations in the combustion chamber were out of phase from those in the plenum, and the resulting changing pressure difference caused the axial velocity at the burner nozzle to fluctuate. Associated swirl number fluctuations convected downstream at the mean flow velocity, deforming the helical vortex locally in the process. The deformations caused the flame to displace, closing the feedback loop.

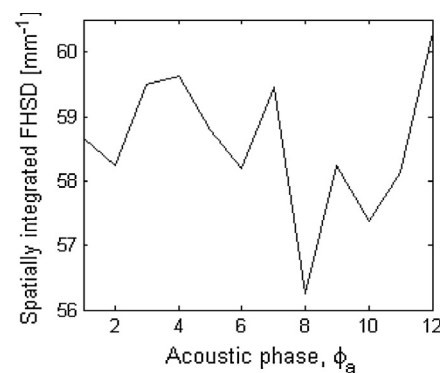
The phase relationship between the pressure oscillations, heat release oscillations, deformation of the HVC, and swirl number waves were further investigated, and it was shown that the phase between the heat release oscillations could be expressed as the sum of two independent phases:

1. The phase between the acoustic cycle and the swirl number oscillations, and
2. the phase between the swirl number oscillations and the heat release oscillations.

The former was then quantified using a simplified acoustic model making use of Helmholtz resonator theory, and was found to agree well with experimental results. In this study, data from numerical experiments was used to fit the model parameters, though it is theoretically possible to derive these parameters from the combustor geometry and properties of the mixture gases. This will be treated in future work.



(a) Instantaneous local flame extinctions.



(b) Net FHSD for case 6.

**Fig. 22.** Flame holes (a) used to compute the net flame hole surface density (b). Flames are represented as blue lines, while the flame holes are shown in magenta. Note that the net FHSD is not periodic over the acoustic cycle. (For interpretation of the references to color in this figure legend, the reader is referred to the web version of this article.)

The phase between the swirl number oscillations and the heat release oscillations was shown to be related to the speed at which the swirl wave convected from the burner nozzle. An increase in this speed meant that it took less time for the swirl number wave to convect downstream from the nozzle exit plane to any given point along the helical vortex, thereby reducing the time and phase delay between the swirl number fluctuations at the nozzle, the HVC's deformation, and the associated heat release oscillations. Quantitative prediction of these phase relationships are left for future work.

## Acknowledgment

This work was supported by NSERC under Grants RGPIN 413232 and STPGP 43036.

## Appendix A. Quantification of local flame extinction

Periodic local flame extinctions were quantified by computing the flame hole surface density (FHSD). Using the flame fronts obtained with the algorithm of Section 3.2, local flame extinctions were approximated by tracing a line between the extremities of two flame fronts. Figure 22a shows the flame fronts (blue) and corresponding local extinctions (magenta) of an instantaneous flame image for Case 6. These approximate flame extinctions were expressed statistically by the FHSD, computed using the same algorithm as for the FSD, and were found to vary by only a small amount in a random fashion over the thermo-acoustic cycle as shown in Fig. 22b. It should be noted that flame holes do not refer to circular, closed, flames that surround regions of incombustible gases. Rather, flame holes represent areas along the flame sheet where the fluid is not reacting, thereby producing a hole in the flame surface. If this were to oscillate over the thermo-acoustic cycle, it would likely affect the global heat release rate in the process.

## References

- [1] S.M. Correa, Combust. Sci. Technol. 87 (1993) 329–362.
- [2] S.M. Correa, Proc. Combust. Inst. 27 (1998) 1793–1807.
- [3] A. Lefebvre, Gas Turbine Combustion, second ed., Taylor and Francis, 1999.
- [4] S.M. Candel, Proc. Combust. Inst. 29 (2002) 1–28.
- [5] T.C. Lieuwen, V. Yang, Combustion Instabilities in Gas Turbine Engines: Operational Experience, Fundamental Mechanics, and Modeling, AIAA, 2005.
- [6] N. Docquier, S. Candel, Prog. Energy Combust. Sci. 28 (2002) 107–150.
- [7] I. Emiris, J.H. Whitelaw, Combust. Sci. Technol. 175 (2003) 157–184.
- [8] A.P. Dowling, A.S. Morgans, Ann. Rev. Fluid Mech. 37 (2005) 151–182.
- [9] A. Boureila, F. Baillot, Combust. Flame 114 (1998) 303–318.
- [10] D. Durox, S. Ducruix, S. Candel, Combust. Flame 125 (2001) 982–1000.
- [11] S.-Y. Lee, S. Seo, J.C. Broda, S. Pal, R.J. Santoro, Proc. Combust. Inst. 28 (2000) 775–782.
- [12] V.G. McDonell, G.S. Samuels, Meas. Sci. Technol. 11 (2000) 870–886.
- [13] Y. Deguchi, M. Noda, Y. Fukuda, Y. Ichinose, Y. Endo, M. Inada, Y. Abe, S. Iwasaki, Meas. Sci. Technol. 13 (2002) R103–R115.
- [14] P. Griebel, P. Siewert, P. Jansohn, Proc. Combust. Inst. 31 (2007) 3083–3090.
- [15] U. Stopper, W. Meier, R. Sadanandan, M. Stöhr, M. Aigner, B. Bulat, Combust. Flame 160 (2013) 2103–2118.
- [16] P. Strakey, S.D. Woodruff, T.C. Williams, R.W. Schefer, AIAA J. 46 (2008) 1604–1613.
- [17] S. Dhanuka, J.E. Temme, J.F. Driscoll, H.C. Mongia, Proc. Combust. Inst. 32 (2009) 2901–2908.
- [18] N. Noiray, D. Durox, T. Schuller, S. Candel, J. Fluid Mech. 615 (2008) 139–167.
- [19] P. Palies, D. Durox, T. Schuller, S. Candel, Combust. Flame 158 (2011) 1980–1991.
- [20] S. Ducruix, D. Durox, S. Candel, Proc. Combust. Inst. 28 (2000) 765–773.
- [21] M. Fleifil, A.M. Annaswamy, Z.A. Ghoneim, A.F. Ghoneim, Combust. Flame 106 (1996) 487510.
- [22] T. Schuller, D. Durox, S. Candel, Combust. Flame 135 (2003) 525–537.
- [23] T. Lieuwen, Proc. Combust. Inst. 30 (2005) 1725–1732.
- [24] F. Baillot, D. Durox, R. Prud'homme, Combust. Flame 88 (1992) 149–168.
- [25] L. Boyer, J. Quinard, Combust. Flame 82 (1990) 51–65.
- [26] G. Borghesi, F. Biagioli, B. Schuermans, Combust. Theory Modell. 13 (2009) 487–512.
- [27] T. Komarek, W. Polifke, J. Eng. Gas Turbines Power 132 (2010). Article ID: 061503.
- [28] J. Ranalli, C. Martin, P. Black, U. Vandsburger, R. West, J. Propul. Power 25 (2009) 1350–1354.
- [29] P. Palies, T. Schuller, D. Durox, S. Candel, Proc. Combust. Inst. 33 (2011) 2967–2974.
- [30] B. Jones, J.G. Lee, B.D. Quay, D. Santavicca, K. Kim, S. Srinivasan, in: Proceedings of the ASME Turbo Expo 2010, pp. 323–333.
- [31] A.M. Steinberg, I. Boxx, M. Stöhr, W. Meier, C.D. Carter, AIAA J. 50 (4) (2012) 952–967.
- [32] A.M. Steinberg, I. Boxx, M. Stöhr, C.D. Carter, W. Meier, Combust. Flame 157 (2010) 2250–2266.
- [33] A.M. Steinberg, C.M. Arndt, W. Meier, Proc. Combust. Inst. 34 (2013) 3117–3125.
- [34] R. Weber, J. Dugue, Prog. Energy Combust. Sci. 18 (1992) 349–367.
- [35] C.O. Paschereit, E. Gutmark, W. Weisenstein, Phys. Fluids 11 (1999) 2667–2678.
- [36] O. Lucca-Negro, T. O'Doherty, Prog. Energy Combust. Sci. 27 (2001) 431–481.
- [37] S. Roux, G. Lartigue, T. Poinsot, U. Meier, C. Bérat, Combust. Flame 141 (2005) 40–54.
- [38] C.E. Cala, E.C. Fernandes, M.V. Heitor, S.I. Shtork, Exp. Fluids 40 (2006) 267–276.
- [39] S. Wang, V. Yang, G. Hsiao, S.-Y. Hsieh, H.C. Mongia, J. Fluid Mech. 583 (2007) 99–122.
- [40] N. Syred, Prog. Energy Combust. Sci. 32 (2006) 93–161.
- [41] Y. Huang, V. Yang, Prog. Energy Combust. Sci. 35 (2009) 293–365.
- [42] A. Lacarelle, T. Faustmann, D. Greenblatt, C.O. Paschereit, O. Lehmann, D.M. Luchtenburg, B.R. Noack, J. Eng. Gas Turb. Power 131 (2009) 031504.
- [43] P. Iudiciani, C. Duwig, Flow Turb. Combust. 86 (2011) 639–666.
- [44] N. Syred, K.R. Dahmen, AIAA J. Energy 2 (1) (1978) 8–15.
- [45] C.M. Arndt, A.M. Steinberg, I. Boxx, W. Meier, M. Aigner, in: Proceedings of the ASME Turbo Expo, Glasgow, UK, 2010, pp. T2010–22830.
- [46] W. Meier, P. Weigand, X. Duan, R. Giezendanner-Thoben, Combust. Flame 150 (2007) 2–23.
- [47] P. Weigand, W. Meier, X.R. Duan, M. Aigner, J. Eng. Gas Turb. Power 129 (2007) 664–671.
- [48] G. Lartigue, U. Meier, C. Bérat, Appl. Therm. Eng. 24 (2004) 1583–1592.
- [49] J. Galpin, A. Naudin, L. Vervisch, C. Angelberger, O. Colin, P. Domingo, Combust. Flame 155 (2008) 247–266.
- [50] B. Fiorina, R. Vicquelin, P. Auzillon, N. Darabiha, O. Gicquel, D. Veynante, Combust. Flame 157 (2010) 465–475.
- [51] B. Franzelli, E. Riber, L.Y.M. Gicquel, T. Poinsot, Combust. Flame 159 (2012) 621–637.
- [52] S.H. Im, Caractérisation des instabilités thermoacoustiques dans les chambres de combustion à gaz (2012).
- [53] V. Rokhlin, A. Szlam, M. Tygert, SIAM J. Matrix Anal. Appl. 31 (2009) 1100–1124.
- [54] A.M. Steinberg, I. Boxx, C.M. Arndt, J.H. Frank, W. Meier, Proc. Combust. Inst. 33 (2011) 1663–1672.
- [55] P. Palies, D. Durox, T. Schuller, S. Candel, Combust. Flame 157 (2010) 1698–1717.
- [56] P. Palies, T. Schuller, D. Durox, L.Y.M. Gicquel, S. Candel, Phys. Fluids 23 (2011) 037101.
- [57] L.E. Kinsler, A.R. Frey, Fundamentals of Acoustics, John Wiley & Sons, New York, 1962.